Large spatial variations in the frontal mass budget of a Greenland tidewater glacier

Till J. W. Wagner[1], Fiamma Straneo[2], Clark G. Richards[3], Donald A. Slater[2], Laura A. Stevens[4], Sarah B. Das[5], and Hanumant Singh[6]

[1]Department of Physics and Physical Oceanography, University of North Carolina Wilmington, NC 28403, USA
[2]Scripps Institution of Oceanography, University of California at San Diego, La Jolla, CA 92093, USA
[3]Bedford Institute of Oceanography, Fisheries and Oceans Canada, Dartmouth, NS B2Y 4A2, Canada
[4]Lamont-Doherty Earth Observatory, Columbia University, Palisades, NY 10964, USA
[5]Department of Geology and Geophysics, Woods Hole Oceanographic Institution, Woods Hole, MA 02543, USA
[6]Department of Electrical & Computer Engineering, Northeastern University, Boston, MA 02115, USA

Correspondence: Till J. W. Wagner (wagnert@uncw.edu)

Abstract. We investigate the frontal mass budget of a medium-sized tidewater glacier in western Greenland. This is done by comparing the seasonal retreat of the glacier to ice advection and ablation along the front. Frontal ablation is partitioned into calving and submarine melting, both of which are estimated from in situ observations. We observe large spatial variability in all mass budget terms along the glacier front. In particular, we find that the ablation of the glacier front is characterized by two main regimes: melting dominated versus calving dominated. While melting-dominated segments appear to be associated with subglacial discharge plumes, calving-dominated regions occur outside such plumes. The melting-dominated segments are rather localized, and the majority of ablation is estimated to occur in the form of calving. However, we stress the large uncertainty in melt rate estimates and consider the possibility that current parameterizations substantially underestimate melting. Finally, we argue that localized melt incisions into the glacier front can be significant drivers of calving. Our results suggest a complex interplay of melting and calving marked by high spatial variability along the glacier front. Understanding the impact of such local variability on larger scale ice dynamics may help guide future mass balance projections for tidewater glaciers.

1 Introduction

The retreat of Greenland's tidewater glaciers may be among the most noticeable manifestations of a changing global climate (Carr et al., 2017). Tidewater glaciers present an important boundary between the ocean and the Greenland ice sheet; they act as thermodynamic buffers as well as mechanical buttresses (Rignot and Thomas, 2002; Howat et al., 2007; Nick et al., 2009). The speed-up of the Greenland ice sheet observed since the year 2000 (Howat et al., 2008; Moon et al., 2012) has likely been caused (at least to some degree) by the thinning of the glaciers' termini (Vieli and Nick, 2011) and, in some cases, the disappearance of their floating tongues (Holland et al., 2008; Wilson et al., 2017). The processes that determine the flux balance at the glacier front therefore impact the ice sheet as a whole, yet a comprehensive understanding of these processes remains elusive. Increased ocean and air temperatures are expected to further increase the rates of glacier retreat in the coming decades (Joughin et al., 2012; Nick et al., 2013), lending additional weight and urgency to the study of calving front dynamics. For a retreating

glacier, the delivery of upstream ice to the terminus is outweighed by the loss of ice due to ablation. At tidewater glaciers this frontal ablation occurs predominantly through two distinct processes: submarine melting and calving. The submarine melting of the glacier front – "melt" hereafter – is a continuous (though seasonally varying) process, determined largely by the local ocean temperatures and water velocities (Holland and Jenkins, 1999; Jackson and Straneo, 2016). The main challenge

5   in constraining melt rates at glacier fronts therefore lies in measuring the ocean properties at these hard-to-reach ice–ocean interfaces, and finding appropriate parameterizations that translate these observations to melt rates. The continued scarcity of such observations results in large uncertainties in current melt parameterizations (Straneo and Cenedese, 2015).

Calving, by contrast, is a discontinuous and highly complex process which is influenced by a multitude of environmental factors, as well as the condition of the ice itself (Benn et al., 2007). In recent years, much effort has been dedicated to studying

10   the calving of tidewater glaciers (see the review by Benn et al., 2017), yet a comprehensive understanding of what processes and variables determine the frequency and magnitude of calving events remains elusive.

Oftentimes calving and melt fluxes are not considered separately, but rather as a single ablation term, in particular when derived from satellite imagery (Luckman et al., 2015). Previous studies of explicit calving activities of Greenland's tidewater glaciers have typically been limited to visible daylight hours (see, for example, the calving event catalogue of Åström et al.,

15   2014), or somewhat indirect detection methods such as teleseismicity (Veitch and Nettles, 2012).

Finally, the calving and melt fluxes of glaciers are oftentimes described by single mean values (Rignot et al., 2016). However, both melting and calving can vary substantially along the front of a glacier, with largely unknown implications for the overall stability of a glacier front. For example, submarine melt is enhanced by an order of magnitude in the vicinity of subglacial discharge plumes (Slater et al., submitted), leading to pronounced undercutting and incision into the ice front (Fried et al.,

20   2015). Spatially resolving these differences is challenging, and in particular spatial calving distributions are difficult to obtain.

Here we use a multifaceted dataset to quantify the relative contribution of calving and melting and their spatial variability along a glacier front. The dataset consists of both in-situ and remotely-sensed observations of the front of Saqqarliup Sermia, a mid-sized Greenland tidewater glacier. The data is unique in its detail, close proximity to the glacier front, and in that it contains observations of all of the main physical quantities of interest. The dataset consists of (i) detailed bathymetry at the

25   glacier front, (ii) high-resolution ice-surface elevations, (iii) InSAR-derived ice-velocities at and upstream from the glacier front, (iv) a continuous 3-week calving event catalogue, (v) local hydrographic measurements that allow for estimates of melt rates, and (vi) multibeam sonar imagery of the underwater shape of the glacier front. The spatial and temporal concurrence of these observations allows us to compare and contrast the individual components that make up the frontal mass budget of the glacier.

30   2   Field campaigns and physical setting

Saqqarliup Glacier and the adjacent Sarqardleq Fjord were visited during two field seasons in the summers of 2012 and 2013. The fjord is a tributary to the Ilulissat Icefjord, with the north-west facing front of the glacier (Fig 1) located 30 km south-east of Ilulissat Icefjord. At the glacier front, the fjord is about 5 km wide and the terminus is mostly, if not completely, grounded.
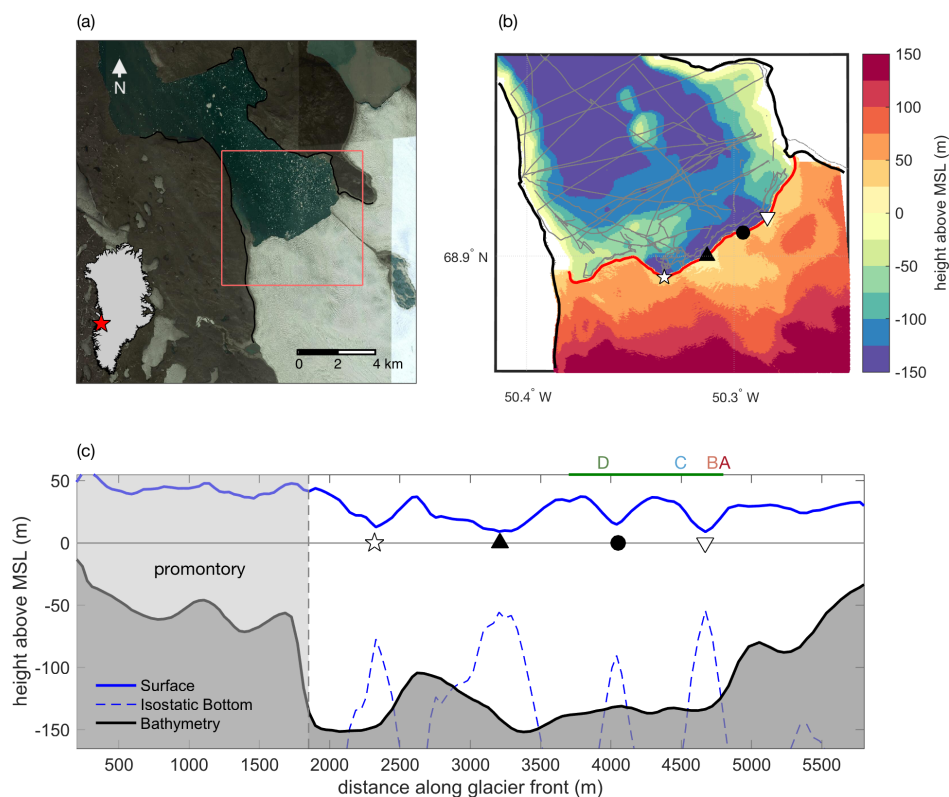
Figure 1. (a) Landsat-8 image of the lower part of Saqqarliup Sermia, and Sarqardleq Fjord. The inset of Greenland shows the location of the glacier. (b) Gridded bathymetry from in-situ observations (readings indicated by gray dots). Also shown is the surface height from ArcticDEM (Digital Elevation Map created by the Polar Geospatial Center from DigitalGlobe, Inc. imagery). Red line shows the front position on 9 July 2013. (c) Surface height (blue) and bathymetry (black) along glacier front (following the red line in panel b). Also shown is the isostatic bottom of the ice (blue dashed). Locations of two main plumes are highlighted in panels (b) and (c) by ☆ and ▽; two additional surface dips are indicated by ▲ and ●. The green horizontal line above panel (c) and the letters A-D indicate the locations of the front profiles shown in Fig 7.

Since 2004, the main north-eastern part of the glacier has been retreating more rapidly than the south-western section, which now juts out by almost 1 km from the rest of the glacier front (Fig S2). This part of the glacier, which we refer to as the "promontory" (Fig 1), is grounded in shallow bathymetry and features tall ice cliffs (40–50 m above mean sea level, see Section 2.2). Overall, the glacier advanced slightly between 1975 and the mid-1990s, but experienced an accelerating retreat until 2016 (Fig S2; Stevens et al., 2016). The front position has been relatively stable from 2016 to 2018.

The 2012 survey, described by Stevens et al. (2016), revealed the presence of two main subglacial discharge plumes along the glacier front which, in turn, drained the two dominant catchment basins. The plume entering the fjord at the eastern edge of the promontory (Fig 1) has an order of magnitude greater drainage and can result in an outcropping surface pool (Mankoff et al.,

2016). We refer to this as the "main" plume. While this plume appears to be a yearly recurring feature, it is likely amplified in some years by the cyclical drainage of the large ice-dammed lake Tininnilik located to the south-west of the promontory (Kjeldsen et al., 2017). We note that the dramatic retreat of the glacier front in 2015 coincided with a major drainage event of lake Tininnilik (Kjeldsen et al., 2017). The second recurring plume is located closer to the north-eastern margin of the glacier
5   (Fig 1), which we'll refer to as the "secondary" plume.

In what follows, we use bathymetry data from both years, while the other in-situ observations were mostly collected during the 2013 season (see Stevens et al., 2016; Mankoff et al., 2016, for further details on the field campaigns).

2.1   Bathymetry

The bathymetry of Sarqardleq Fjord was first mapped in detail during these two field seasons and the immediate bay in front
10 of the terminus was found to feature depths of $40 - 150$ m (Stevens et al., 2016). These initial results were limited to data from REMUS and shipboard ADCP, which did not get closer than ~ 200m to the glacier front. Here, we supplement this data with several additional near-terminus datasets from the 2013 field campaign (Fig S1), which allows for a detailed bathymetry map along the grounding line. The new data consists of circa 39,000 depth readings taken with Jetyak-mounted (Kimball et al., 2014) and ship-mounted ADCPs. In addition, there are approximately 6000 readings from the ship-mounted NMEA bottom-
15 range profiler and 6 readings from XCTDs deployed in the otherwise undersampled region of the main plume. Most of these readings are between 10–100 m from the glacier front.

Fig 1c shows the new bathymetry at the glacier front as a function of x, the distance along the glacier front. The bathymetry can be split into two main regimes: For $x < 1800$ m (the promontory) the glacier is grounded in shallow waters and its surface heights are elevated substantially above flotation. From here on, we refer to the eastern part of the glacier ($x > 1800$ m) as
20 the 'main' glacier. In 2013, the front of the promontory was grounded on a sill that runs parallel to the glacier front. This sill coincides approximately with the furthest advance of the glacier in 1992 (Stevens et al., 2016). By 2013 the main glacier had retreated ~ 500 m from the sill, but the promontory was still perched on it in bathymetry of 60 m depth or less (Fig 1c). Since 2013, this part of the glacier front has also retreated by several hundred meters (Fig S2). In 2013, the main part of the glacier front was in waters of depth 40-150 m. A pronounced dip in bathymetry – suggestive of a subglacial channel – is found near the
25 location of the main plume ($x = 2000 - 2400$ m). A number of smaller dips are observed between $x = 3400 - 4700$ m. Beyond 4700 m the water depth decreases as one approaches the northeastern shoreline.

2.2   Glacier surface topography

We obtained a digital elevation map (DEM) from an ArcticDEM overflight on 22 March 2013, which covers the full span of the Saqqarliup glacier front and some of the upstream region (Fig 1). The DEM has a horizontal resolution of 2 m and is capable
30 of resolving individual crevasses on the glacier surface.

The DEM shows that the front of the glacier is heavily crevassed and has several pronounced dips in the surface elevation at the terminus. The ice cliff is highest (up to 50 m) and most uniform in the region of the promontory, while the main part of the
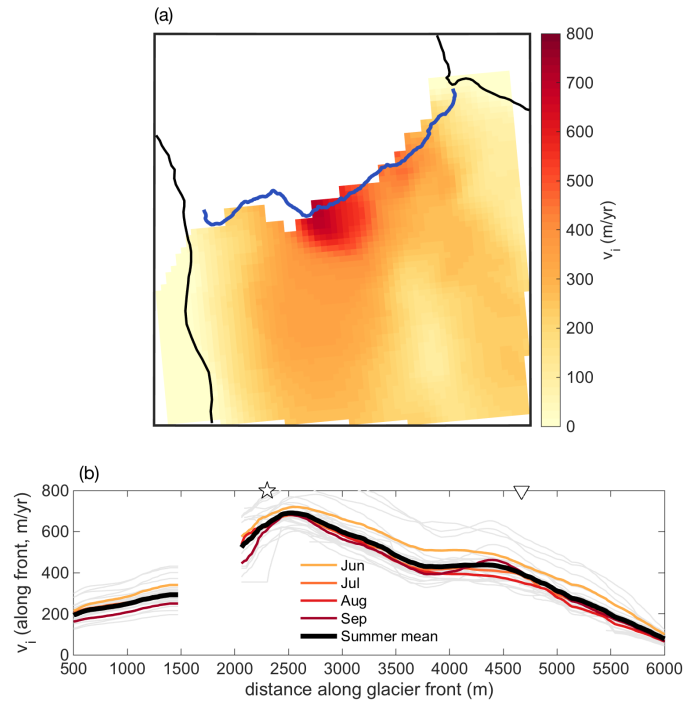
Figure 2. (a) InSAR Ice velocity data near the glacier front. Shown are mean summer (June–September) values averaged over 28 velocity fields, collected during 2012–2014. Note that there is a consistent data gap near the promontory. The shading represents the horizontal velocity magnitude. (b) Velocity profiles along the glacier front. Here, as in all figures, the perspective is with the direction of ice flux into the page. The faint gray lines show the 28 individual velocity fields. Also indicated are the approximate locations of the two plumes (☆, ▽).

glacier is much more variable with four distinct depressions that reach below 10 m surface elevation (indicated by symbols in Fig 1).

The coincident high-resolution surface elevation and bathymetry data near the terminus enables us to compute the total ice thickness along the glacier front, $H(x)$, which allows for an estimation of the total ice flux (discussed in Section 3).

5   The data suggests that the terminus might be floating at several locations: the four highlighted surface depressions at the glacier front are all low enough to raise the isostatic bottom of the ice above the local sea floor. The locally-isostatic bottom of the ice is indicated in Fig 1c (blue dashed line). Here we assume an average ice density of 883 kg m^{-3}, obtained as a mean of low and high values commonly used for glacier and ice shelf front densities, namely 850 kg m^{-3} (Silva et al., 2006) and 917 kg m^{-3} (pure ice). It should be noted that the surrounding ice and the associated stiffness of the glacier will likely prevent the ice

10   from assuming local isostasy everywhere along the glacier front. However, the isostatic bottom can be used to compute a lower bound on the ice thickness in regions where the ice may be floating. It may be speculated that the ice appears to be floating in these regions due to undercutting by submarine melt (which in turn is associated with rising discharge plumes, as discussed
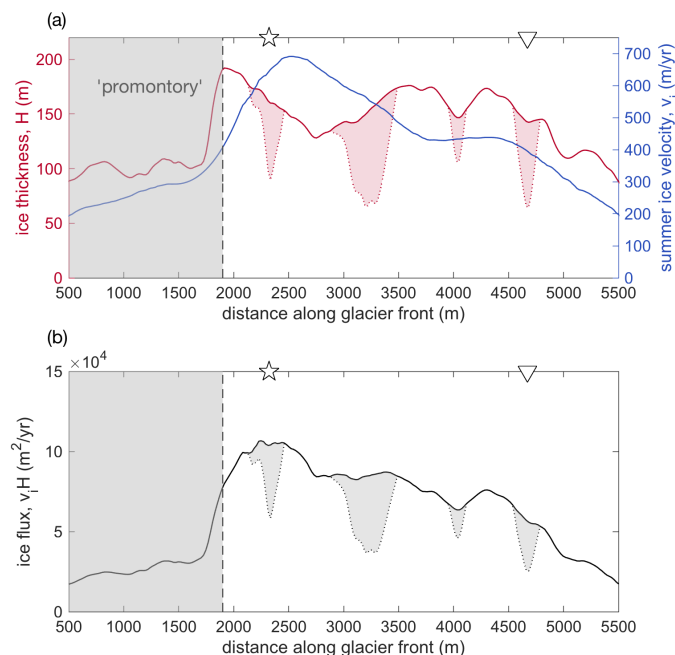
Figure 3. (a) Mean July ice velocity along the glacier front in blue (right vertical axis). Here we used cubic interpolation to fill the data gap shown in Fig 2. In blue (right vertical axis) is shown the estimated ice thickness along the glacier front, obtained by computing the difference of the surface and bathymetry profiles of Fig 1(c). The dotted red line shows the ice thickness at the glacier front assuming the ice is locally in isostatic equilibrium everywhere. (b) Ice flux along the glacier front (in black), computed from the product of velocity and thickness (shown in panel a). The shaded gray areas under the curve show the ice-flux range due to potential flotation. This is a result of the thickness ranges indicated as red shaded areas in panel a. Also indicated are the approximate locations of the two known plumes ($\star$, $\triangledown$), which coincide with two areas of possible flotation.

in Section 4.2). The ice would be grounded everywhere else. In particular, the ice surface is elevated substantially beyond its isostatic height in the region of the promontory.

3 Ice flux and retreat

3.1 Ice velocity and advective ice flux

5   Several dozen ice-velocity reconstructions of the lower part of the glacier are available for the years 2009 – 2015 from InSAR data (Joughin et al., 2011). The mean flow velocity at the glacier front (averaged over all available fields) is ~ 350 m yr^{-1} with minima at the edges of the glacier. There is a notable peak in ice velocity (up to 750 m yr^{-1}) near the location of the main plume (Fig 2). A second region of elevated velocities is found near $x = 4500$ m and is more pronounced further upstream from the glacier front. The drainage location of this second stream coincides with that of the secondary plume. It is worth noting that
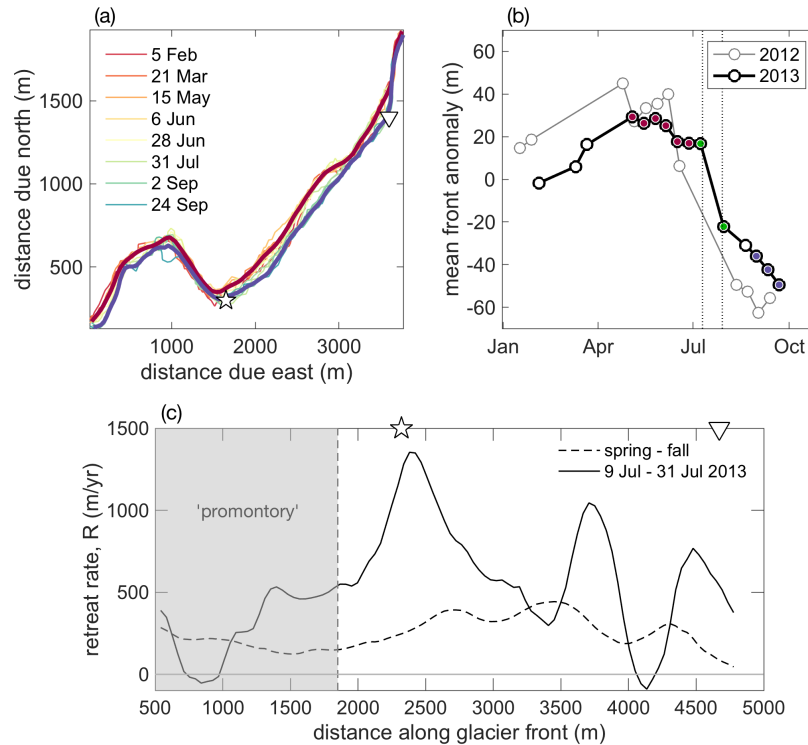
Figure 4. Seasonal advance and retreat of glacier front. (a) 15 front profiles acquired from February to September 2013; the legend highlights every 2nd profile. The thick red and blue profiles represent the May–June and Sept averages, respectively. Also indicated are the location of the two plumes ($\star$, $\triangledown$). (b) Mean front position, shown as an anomaly from the yearly mean position. 2012 values are shown in gray, 2013 in black. The spring profiles used in panel (a) are highlighted in red, fall profiles in blue. The vertical dotted lines demarcate the period from 12 to 31 July during which calving was observed. (c) Retreat rates, $R(x)$, along the glacier front. The dashed line represents the spring–fall mean retreat rates; the solid line that of 9 to 31 July, computed from the profiles marked green in panel (b).

the spatial distribution of velocities was remarkably consistent during summer months from 2012–2014 (Fig 2b), followed by a substantial overall slowdown in 2015 (not shown). This slowdown has been linked to a major drainage event of lake Tininnilik (Kjeldsen et al., 2017). In what follows, we will consider the 2012–2014 mean July velocity profile along the glacier front. Using the mean summer (May–September) velocities instead does not change the results appreciably.

5   The magnitude of the summer ice velocity along the glacier front, $v_i(x)$, shown in Fig 2b, together with the ice thickness profile $H(x)$, allows for an estimate of total advective ice flux (Fig 3). This assumes plug flow, i.e., that the ice velocity is approximately constant from the surface to the ice–bedrock interface, which is considered a good approximation for fast-flowing tidewater glaciers (Meier and Post, 1987). The uncertainty in ice thickness associated with the glacier potentially floating at several points along the front is illustrated by the shaded areas in Fig 3. In the figure, the upper bound of the ice
10   thickness assumes a fully grounded glacier front, while the lower (dashed) bound assumes local isostasy everywhere. The ice
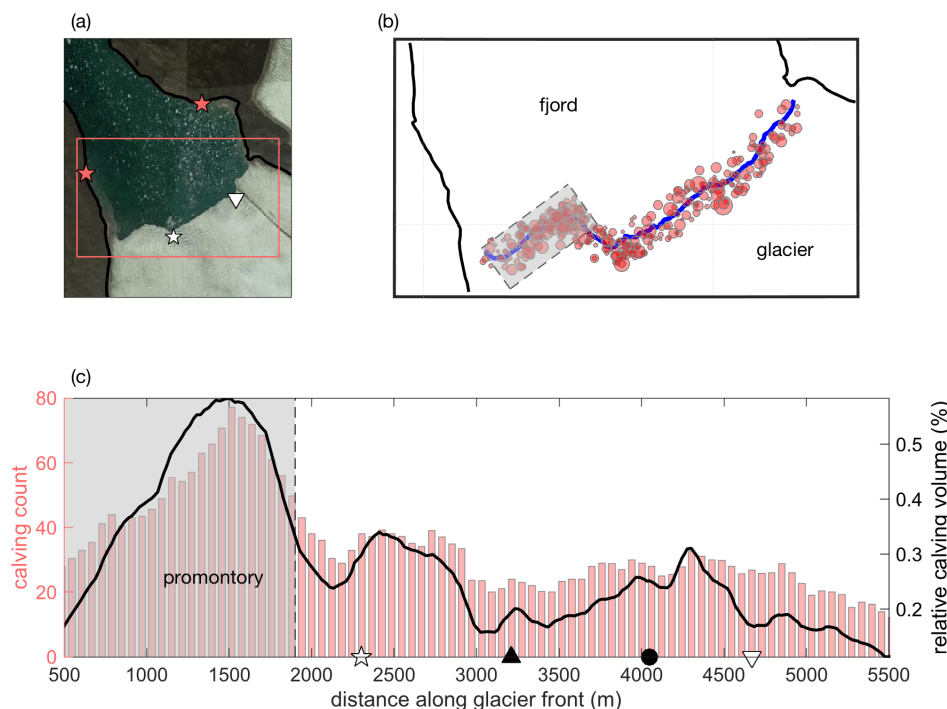
Figure 5. (a) Close-up of glacier front and adjacent fjord, with the red rectangle outlining the region of interest (panel b) and red stars indicating the location of the wave moorings; (b) spatial calving distribution as estimated from pressure sensor data; the shaded rectangle indicates the promontory; (c) calving count along glacier front, obtained as total number of calving events detected within a 300 m running window along the glacier front (red bars, left axis). Also shown is an estimate for the relative calving volume, computed from the product of the frequency of calving events and the corresponding magnitudes of the detected waves (black line, right axes). Plume and surface dip locations are indicated as in previous figures.

flux is highest when assuming a fully grounded glacier, while a partially floating glacier front would have a correspondingly reduced flux.

3.2 Changes in glacier front position

Superimposed on the aforementioned long-term retreat of the glacier front over the past decades (Fig S2) we observe a sea-
5 sonal advance–retreat cycle during 2012 and 2013 (Fig 4). A total of 27 front positions between January–October 2012 and January–October 2013 were digitized from TerraSAR-X satellite images. The 15 profiles from 2013 are shown in Fig 4a. Both years exhibit a clear, albeit modest, seasonal cycle in terminus migration, with a spatial-mean advance of roughly 30 m from January through April/May, followed by a more rapid retreat from June to September of circa 80 m (Fig 4b). However, there is substantial along-glacier variability in this cycle. Near the edges of the glacier, and in particular at the promontory, the glacier
10 exhibits a much reduced advance–retreat cycle, and more variable regions are found in the main dynamic section of the glacier.

We define $R(x)$ as the rate of retreat of the glacier front at location x, in m yr^{-1}. $R(x)$ is computed as the rate of retreat perpendicular to the initial glacier front. The most rapid retreat in 2013 was observed at the time of the July study period. Fig 4b shows the spatial-mean seasonal retreat anomalies for 2012 and 2013, with profiles from 9 July and 31 July 2013 highlighted in green. Such rapid retreat is spatially highly variable (Fig 4c) and likely strongly impacted by sporadic but large individual calving events. Longer-term mean retreat rates, computed from average spring and fall glacier front positions (highlighted in Fig 4 in red and blue, respectively) may therefore be more representative on longer time scales.

4   Ablation

In order for the mass budget along the glacier front to be balanced, the sum of advective ice flux and frontal retreat must be balanced by total ablation (i.e., by the sum of melting and calving fluxes). Here we consider a steady state, vertically averaged balance. At a given point x along the glacier front this can be written as

$$H\left(R+v_i\right) = D\bar{M} + C. \tag{1}$$

The terms on the left hand side (retreat rate and advective ice flux) have been discussed in Section 3. The first term on the right represents the ice loss due to submarine melting, where D is the draft of the glacier and $\bar{M}$ is the depth-averaged melt rate. $\bar{M}$ is derived from in-situ hydrographic observations, in concert with a high-resolution numerical model (see Section 4.2). The final term on the right hand side of equation (1) is the volume loss due to calving. This is estimated from in-situ pressure sensors (see Section 4.1), and presents the least well constrained term of equation (1).

In what follows we consider the volume flux across the glacier front during the summer of 2013. We make the assumption that this flux was steady during the study period and ignore time-dependencies of the individual terms in equation (1).

4.1   Calving frequency and distribution

Calving events were detected over a 19-day period from 12 July to 31 July 2013, using two pressure sensor moorings located on the western and eastern banks of the fjord, each at a distance roughly 2 km from the nearest point along the glacier front (Fig 5a). The dispersion of waves that are created by individual calving events can be inverted to estimate the distance between the mooring and the origin of the wave. Wave packets that are detected by both moorings can be used to triangulate the time and position of the corresponding calving event (Minowa et al., 2018). The method has been validated against a photography-derived calving record by and good correspondence was observed (not shown). The study by Minowa et al. (2018) provides a detailed description of the method.

In total, 336 calving events were identified using this method over the period that both sensors were recording. Fig 5b shows the location and an estimated magnitude of the individual events. The calving frequency distribution along the glacier front is illustrated in Fig 5c.

A pronounced peak in frequency is found at the promontory, where shallow bathymetry causes the glacier to be elevated substantially beyond its isostatic height of flotation. With its high ice cliffs the promontory can be regarded as a region that is subject to a rather different calving regime than the rest of the glacier.

For the main part of the glacier, we observe a peak in calving activity at a distance $x \approx 2400$ m along the glacier front, near
5   the concave bend in the glacier front (Fig 5b). A second peak in calving activity is found around $x \approx 4300$m. Both peaks appear slightly offset from the location of the two plumes. The calving activity is lowest at the northeast edge of the glacier.

Even though this dataset presents a rather accurate record of calving frequencies, it remains challenging to infer a total volume of calved ice (Minowa et al., 2018). This is due to the different modes of calving (e.g., ice cliff calving versus submarine calving), as well as the different shapes of calved ice blocks and the differing heights from which they fall (or depths from
10   which they rise). Distinguishing between these events from the pressure sensor data is a difficult task and beyond the scope of this study. The pressure sensors do record an amplitude of the incoming wave packet associated with a given calving event, and assuming that this amplitude is correlated with the size of the calved ice we can estimate a relative calving volume (black curve in Fig 5b). However, since a small cone-shaped ice block can act as a more efficient wave generator than a large flat piece of ice (N. Pizzo, personal communication, Bühler, 2007), it is difficult to ascertain a direct relation between wave amplitudes
15   and calving volume. In what follows we therefore only consider the calving frequency record and will scale this record such that the resulting mean calving flux approximately closes the mass budget at the glacier front.

4.2 Submarine melting

The submarine melting regime at Saqqarliup has been studied in detail by Slater et al. (submitted) and is briefly described here. Submarine melt rates are thought to respond primarily to fjord water velocities and temperatures adjacent to the calving front
20   (Holland and Jenkins, 1999). Given the great difficulties of directly measuring submarine melt rates, it is common to instead estimate water velocities and temperatures and then employ a parameterization to estimate melt rates. Slater et al. (submitted) used both data collected close to the calving front and a numerical model to estimate water properties, and thus, submarine melt rates at Sarqardleq Sermia. There is good agreement between the melt rates estimated with the numerical model and with the observations. Here, we only consider the modeled melt rates, which have the advantage of covering the whole extent of the
25   glacier front (unlike rates inferred from observations, which have data gaps in and around the plumes).

The most relevant term for the frontal mass budget is the depth-averaged melt rate (Fig 6b). However, we also consider the possibility for melting to have a dynamic impact on calving, in which case the vertical profile of the melt rates becomes of interest.

There is large spatial variability in submarine melt rates along the glacier front. Submarine melt rates are highest (both in a
30   depth-averaged and maximum sense) within the two plumes where the discharge of buoyant surface meltwater from beneath the glacier gives high water velocities. Outside of the two plumes melt rates are much smaller in a depth-averaged sense, however the lateral circulation excited by the plumes combines with warm surface waters to give high melt rates near the surface outside of the plumes (Slater et al., submitted).

While these melt-rate estimates represent the state-of-the-art in terms of melt-rate modeling, we stress that they are based on a melt-rate parameterization that has not been confirmed by observations, especially for the case of a mostly vertical front of a tidewater glacier. The uncertainty associated with these melt-rate estimates is further discussed in Section 6.
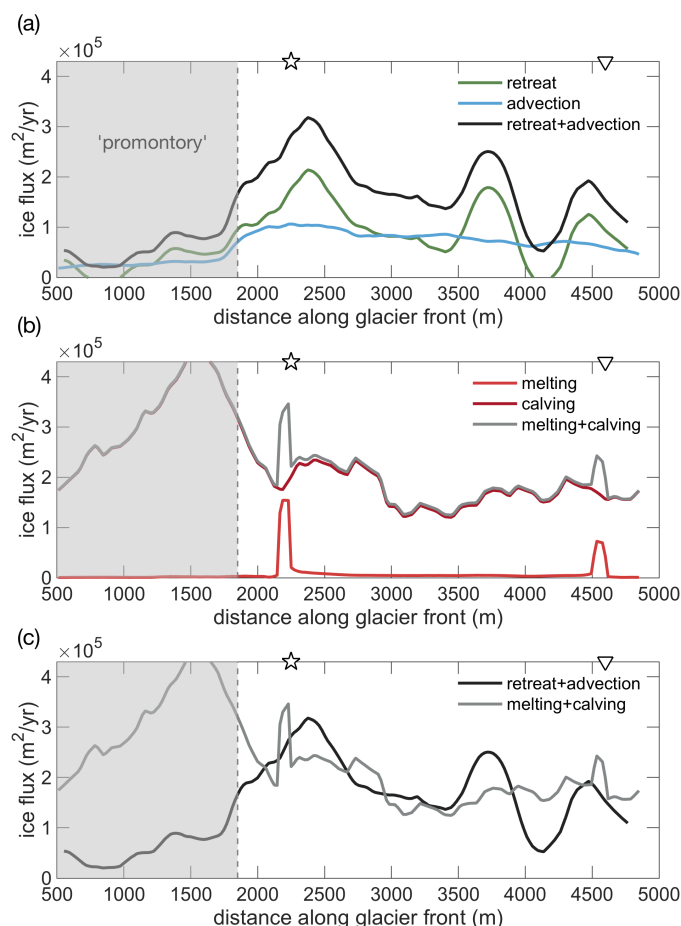
Figure 6. Flux balance along the glacier front. (a) The green line represents the July 2013 retreat rate and the blue line the advective ice flux. The sum of these two terms (black) must be equal to total ablation. (b) Melt flux (red) and calving flux (dark red). The total ablation, i.e., the sum of melting and calving, is shown by the gray line. Note that the calving flux has been scaled to approximately close the budget. (c) Approximate closure of the volume flux budget along the glacier front. The black line shows the sum of ice advection and retreat as in panel (a), while the gray line shows the total ablation as in panel (b).

5   Overall flux balance and spatial variability

5.1   Frontal mass budget

To compare the different terms in the overall mass budget, we consider the retreat rate as computed from the two fronts measured on 9 and 31 July 2013, since this is almost the exact time window of the calving observations (12 – 31 July). For the advection term we use the July average over the years 2012 – 2014, since the July 2013 ice velocity fields have substantial data gaps at the glacier front. However, as discussed above, there is little interannual variability in v_i over these years, so the 3-year mean likely gives a close approximation to the July 2013 velocity field. Front retreat, advective flux, and their sum (i.e., the left hand side of equation 1) are shown in Fig 6a. Melt fluxes, estimated calving volumes, and their sum (i.e., the right hand side of equation 1) are shown in Fig 6b. The two sides of equation 1 are compared directly in Fig 6c.

Integrated along the main part of the glacier front we estimate an ice advection rate of 0.2 ± 0.05 Gt yr^{-1} and a retreat rate of 0.3 ± 0.16 Gt yr^{-1}. The uncertainty in ice advection corresponds to one standard deviation in the spread of mean July ice velocities. The uncertainty in the retreat rate corresponds to one standard deviation in spatial variability between the July 2013 retreat rate and the spring–fall retreat rate. This gives as a best estimate for the total rate of ice loss ~ 0.5 Gt yr^{-1}.

Using the aforementioned melt-rate parameterizations we find a total melting flux of 0.03 Gt yr^{-1}. This would suggest that 94% (0.47 Gt yr^{-1}) of ablation occurs in the form of calving. Thus, the glacier would lose mass almost exclusively due to calving in most places, apart from in localized areas near the subglacial discharge plumes. However, there are large uncertainties associated with the total melt-rate estimate. And even for a small total melt flux, melting may be important for the overall flux balance due to its dynamic impact on calving. These findings are discussed further in Section 6.

5.2   High spatial variability along the glacier front

A striking feature of almost all components of this multipartite dataset is their high spatial variability along the glacier front.

The ice thickness at the front ranges from thin (<40 m) sections near the northeast edge to ~100 m along the promontory and up to 192 m near the main plume, with substantial variations throughout. Overall, we observe a mean thickness of 128 m with a variability of ±38 m (one standard deviation).

We find that the advective flux is suppressed at the promontory and highest near the outflow location of the main plume, with a second smaller peak near the secondary plume (Fig 3).

The retreat rates are overall of comparable magnitude to the advective flux. However, the retreat rates are spatially extremely variable, in particular the observed July 2013 rates, which exhibit three regions of enhanced retreat, two of which are close to the two discharge plumes, with peaks at $x = 2400$ and 4400 m (Fig 4c). Averaged over longer time periods, the retreat rates also become more uniform (as discussed above), which suggests that observations over shorter time periods are more strongly influenced by individual calving events.

Calving frequencies are strongly enhanced at the promontory, which – given the reduced advection and retreat in this area – suggests that calved pieces are in general smaller here. Since we are unable to adequately distinguish between the different calving sizes, the heightened calving activity at the promontory results in a large discrepancy between the estimated total

ablation and the sum of retreat and advection in that region (gray and black curves in Fig 6c). We may also be underestimating the advective flux at the promontory, since we only consider horizontal velocities, and the ice flow may have a non-negligible vertical component as the glacier rides onto the local sill. Even though calving frequencies are overall lower for the main part of the glacier, we observe two local maxima, slightly offset from the plumes (Fig 6b). Some of the lowest calving frequencies

5   are found between the two plumes in the region farthest from both plumes.

The two peaks in depth-averaged melt flux (Fig 6b), co-located with the two discharge plumes, are just offset from the two peaks in frontal retreat and calving. The maximum melt flux value (1.5×10^5 m^2 yr^{-1}) is slightly higher than the mean retreat and advective flux values (1.0×10^5 and 0.8×10^5 m^2 yr^{-1}, respectively). Outside the two plumes the mean melting flux (0.04×10^5 m^2 yr^{-1}) is an order of magnitude lower than inside the plume and than the other budget terms.

10   In order to approximately balance the total ablation with the sum of ice advection and retreat, we scale the relative calving frequencies by a constant factor. This gives a mean calving flux of 1.7×10^5 m^2 yr^{-1}, which is an order of magnitude larger than the estimated mean melting flux of 0.1×10^5 m^2 yr^{-1}.

5.3   Variations in the vertical glacier front profile

A final piece of observational evidence which may help in the interpretation of the results above is provided by point cloud

15   images of the glacier front profile. These were collected during the 2013 field season using an autonomous surface vehicle – the Woods Hole Oceanographic Insitution "Jetyak" (Kimball et al., 2014; Mankoff et al., 2016). Among other instruments, the Jetyak carried a multibeam sonar that was mounted sideways facing the glacier, which collected three-dimensional maps of the underwater portion of the glacier front. Further details of the Jetyak's operation and data can be found in Kimball et al. (2014). Here, we highlight several characteristic frontal profiles. Fig 7 shows a point-cloud transect of the northeastern flank of the

20   glacier, as well as four vertical line profiles at different locations along the transect.

The first two profiles (A and B) are placed near the secondary plume. Both profiles are marked by two features: (i) a sloped upper 20–25 m, which results in the above-water cliff of the glacier being set back by 10–20 m, relative to the most ocean-ward point of the glacier face. (ii) Below 40 m depth we observe up to 10 m of undercutting, such that the protrusion beyond the above-water cliff is most pronounced at depths 20–40 m, and the ice is substantially eroded at greater depths. This is likely

25   caused by the rising subglacial plume which leads to preferential melt of the deeper parts of the glacier front (Fried et al., 2015; Slater et al., 2017). Note that the high turbidity of water within the main plume prevented the Jetyak from surveying the shape of the glacier front occupied by that plume.

Profiles C and D, which are located far from the plume, also feature said underwater ice protrusion, however, they show no signs of undercutting. The presence of such net-buoyant underwater protrusions and their potential impact on calving has been

30   studied previously (Wagner et al., 2014, 2016), and will be discussed further in the next section.

We note that the bathymetry reaches depths of around 130 m for this part of the glacier and the bottom 50 m or so are unfortunately not captured by the multibeam sonar. However, the profiles located near the melt (A and B) can be expected to be further undercut below the observed range (Fried et al., 2015), while profiles C and D likely do not feature such undercutting.
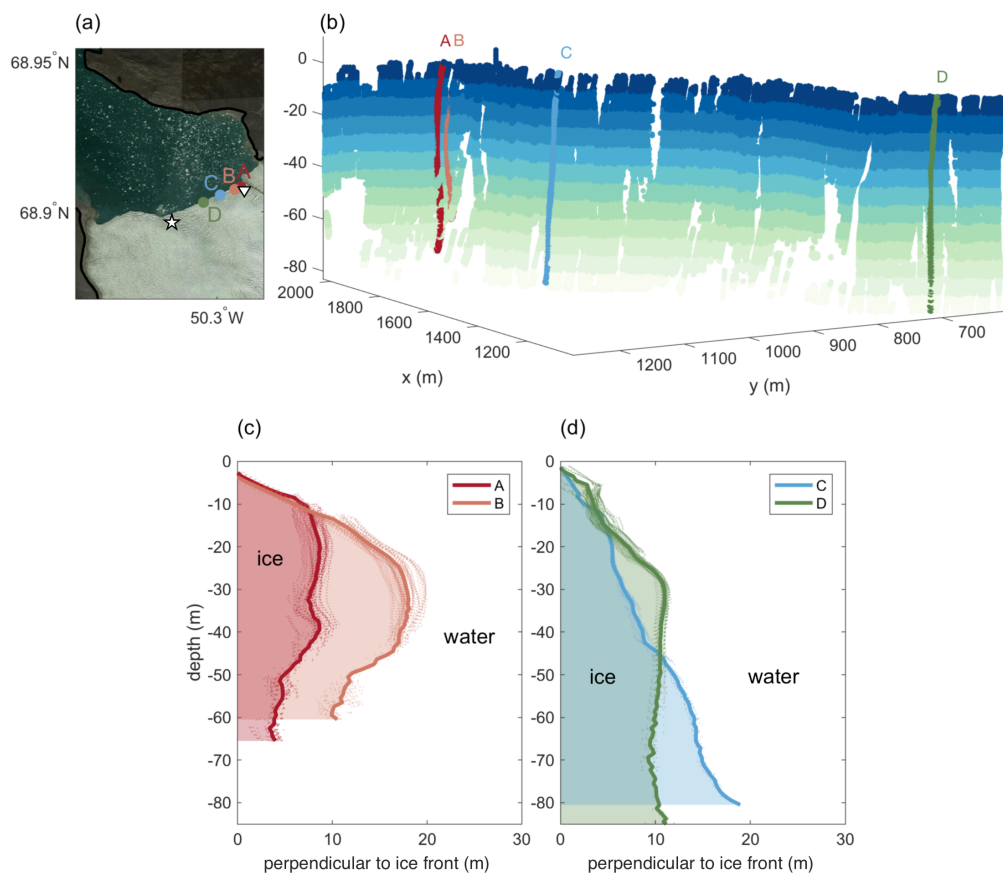
Figure 7. Multibeam sonar data of glacier front from 26 July 2013. (a) Map illustrating the location of the shown multibeam cross-sections A–D and the two plumes (☆, ▽). (b) 3D point-cloud transect showing a part of the eastern side of the glacier (distance along glacier front, ~ 4000 – 4800 m). Data is color-coded by depth below sea level. Indicated are the locations of the four cross-sections A–D shown in panels c and d. (c) Cross-sections A and B near subglacial plume, exhibiting characteristic undercutting. (d) Cross-sections C and D away from plume, showing submarine protrusions without undercutting.

6 Discussion - the role of melting in the frontal mass budget

6.1 Uncertainty in melt rate estimates

The finding that calving appears to make up almost the entire loss of ice is somewhat unexpected, in particular since during the study period the glacier's calving activity was limited to relatively small events, and the fjord was by-and-large devoid of
5 icebergs.

These observations, along with the large uncertainty of the melt-rate parameterization used to convert near-ice ocean properties to melt rates, warrants the consideration of an end-member scenario: suppose that submarine melting accounted for all of the frontal ablation beneath the fjord surface, with calving only removing ice above the water. How would the melt rate parameterization need to be modified in order to achieve this? Scaling the turbulent transfer coefficients in the melt rate parameterization upward by an order of magnitude would increase melt rates by approximately an order of magnitude, allowing the melting outside of the plumes to roughly balance the total loss (Figs 6b and c). We do not think this is realistic however as the melt rates inside the plumes would also increase by an order of magnitude, and this would presumably drive retreat at a much faster rate than observed.

We next consider how water velocity enters the melt rate parameterization. Since plumes drive an entrainment velocity which is ~10% that of the plume velocity (Morton et al., 1956), mean flow velocities outside of plumes will always be approximately an order of magnitude smaller than inside the plumes. One could argue that the mean modeled velocities, particularly outside the plumes, are too small for a number of reasons including coarse model resolution and the lack of tides, surface waves, and calving events which may excite water motion. These factors might crudely be taken into account by placing an additional velocity in the melt-rate parameterization. Such an approach has some precedent with the inclusion of tides beneath ice shelves (Jenkins and Physical, 2010). In order for melting to account for all of the ice loss an additional velocity with magnitude 1 m s^{-1} would have to be added to the parameterization. This appears physically improbable, and perhaps 0.2 m s^{-1} (accounting for ~20% of the ice loss) is more reasonable. Clearly this is an observationally underconstrained discussion. However, it appears worth highlighting that through a reasonable modification of the melt rate parameterization, melting can account for a larger fraction of the ice loss than reported here.

6.2 Dynamic impact of melting on overall ablation

Even if the volume of ice lost through submarine melting is small, melting may still play an important role in the glacier's frontal flux balance: since it is highly focused on discrete regions of the glacier front, melting can lead to sharp incisions in the front profile that may be significant drivers of calving.

Slater et al. (submitted) found that fjord recirculation driven by subglacial discharge plumes can cause substantial near-surface horizontal melting along the glacier front (away from the discharge locations of the plumes). This near-surface melting has in turn been suggested as a potential driver for large calving events at glacier fronts that are floating or close to floating (Wagner et al., 2016): Preferential near-surface melting at the glacier front leads to a horizontal melt incision near the water surface which in turn causes erosion of the above-water ice cliff. As a result, the front of the glacier is left with an underwater protrusion (or "ice foot") as in the profiles C and D of Fig 7. This frontal profile is statically unstable, since the ice foot is net buoyant and exerts bending stresses on the glacier. Calving events occur when such stresses surpass the yield strength of the terminus. This process has also been observed on icebergs in temperate waters (Scambos et al., 2005; Wagner et al., 2014). It is likely that profiles C and D represent sizable ice feet which exert bending stresses that enhance the calving flux in this region.

Furthermore, it is possible that the regions adjacent to the meltwater plumes are more prone to calving since the high melt rates at the plumes cause vertical incisions in the glacier front (Fried et al., 2015). These in turn would reduce the transverse

(i.e., along-front) stability of the terminus, and trigger further calving. A surface expression of such a vertical incision in the glacier front can be found near the main plume in the profile of August 2012 (Fig S2). Considering the particular geometry of Saqqarliup, as the two main plumes drive rapid melt near the two edges of the main part of the glacier, this may cause the entire front between the plumes to be more prone to calving, in particular since we have found this region to be close to (or at)

5   flotation.

In summary, from the observations presented in the previous sections, we propose that there are two distinct regimes driving ablation at Saqqarliup: (a) melting-dominated ablation in spatially confined regions near the discharge plumes, and (b) calving-dominated ablation in the regions away from the plumes (which may nevertheless be enhanced by near-surface horizontal melt incisions). This is further supported by the local minima in calving activity at the location of the two discharge plumes (Fig

10   6b). The two ablation regimes are summarized in the schematic of Fig 8.
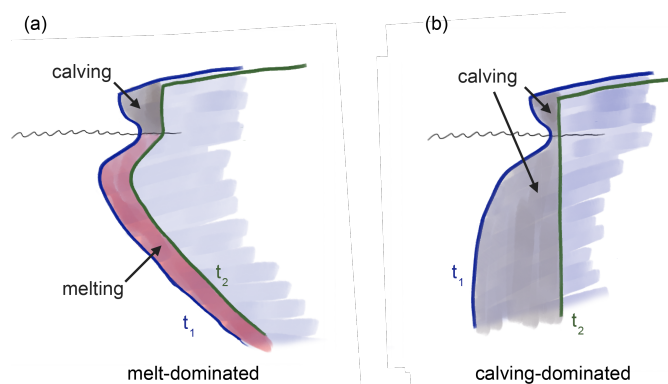
Figure 8. Schematics of two distinct ablation regimes. (a) Melt-dominated regime: the vertical structure of melting due to a rising subglacial discharge plume which entrains warm ambient water results in substantial undercutting of the glacier front (as in profiles A and B in Fig 7). These front profiles likely do not cause large calving events with calving mostly confined to the smaller above-water cliff. Profiles are drawn for an earlier time t_1 and a later time t_2 by which the glacier has retreated mostly due to melting. (b) Calving–dominated regime: here the growth of sizable and buoyant underwater feet (as in profiles C and D in Fig 7) can accelerate calving, with the melt contribution confined to a small region near the water surface. Again, profiles are shown at t_1 and t_2 (pre and post-calving), as part of the "footloose" calving cycle (Wagner et al., 2014).

7   Conclusions

We have presented a multi-faceted dataset of a Greenland tidewater glacier and its surroundings. The unique dataset enables us to investigate the individual terms that determine the flux balance along the glacier front.

We find that the individual terms that comprise the glacier's frontal mass budget are marked by high spatial variability.

15   Ice velocities feature maxima that coincide with troughs in the bathymetry and locations of subglacial discharge plumes. The retreat rates are spatially particularly variable when calculated over shorter periods of time (days to weeks). Spikes and troughs

in glacier retreat rates over such short timescales are likely dominated by somewhat stochastic calving events. Melting, on the other hand, is more consistent throughout the summer and can be expected to only feature gradual changes. Overall, ice loss due to melting, as calculated from commonly used melt-rate parameterizations and observed ocean properties, is an order of magnitude smaller than ice loss due to calving. We note, however, the large uncertainty in the melt rate estimates and stress

5   the possibility that melting could account for a larger proportion of mass loss with modest modifications of the submarine melt rate parameterization.

The spatial variability of the observed processes suggests the presence of two distinct ablation regimes: a melting-dominated one near the discharge plumes and a calving-dominated regime away from the plumes. We suggest that melting, through its horizontal and vertical variability, may play an important role in driving calving, thus having a dynamic effect out of proportion

10 to the fraction of mass lost by melting. If calving is indeed dependent on the localized melt rates, this may have far-reaching implications for the overall stability of the glacier. Understanding the impact of these spatially highly variable processes on ice sheet dynamics should thus be a priority in the study of ice–ocean interactions.

Competing interests.   The authors declare no competing financial interests.

Acknowledgements.   We acknowledge support from the Woods Hole Oceanographic Institution Ocean and Climate Change Institute Arctic

15 Research Initiative, and PLR-1418256, to F. Straneo and S. B. Das. T. J. W. Wagner was further supported by NSF OPP award 1744835. Geospatial support for this work provided by the Polar Geospatial Center under NSF OPP awards 1043681 and 1559691. DEMs provided by the Polar Geospatial Center under NSF OPP awards 1043681, 1559691 and 1542736.

References

Åström, J. A., Vallot, D., Schäfer, M., Welty, E. Z., O'Neel, S., Bartholomaus, T. C., Liu, Y., Riikilä, T. I., Zwinger, T., Timonen, J., and Moore, J. C.: Termini of calving glaciers as self-organized critical systems, Nature Geoscience, 7, 874–878, 2014.

Benn, D. I., Warren, C. R., and Mottram, R. H.: Calving processes and the dynamics of calving glaciers, Earth-Science Reviews, 82, 143–179, 2007.

Benn, D. I., Cowton, T., Todd, J., and Luckman, A.: Glacier Calving in Greenland, Current Climate Change Reports, 3, 282–290, 2017.

Bühler, O.: Impulsive fluid forcing and water strider locomotion, Journal of Fluid Mechanics, 573, 211–236, 2007.

Carr, J. R., Stokes, C. R., and Vieli, A.: Threefold increase in marine-terminating outlet glacier retreat rates across the Atlantic Arctic: 1992–2010, Annals of Glaciology, Vol 27, 1998, 58, 72–91, 2017.

Fried, M. J., Catania, G. A., Bartholomaus, T. C., Duncan, D., Davis, M., Stearns, L. A., Nash, J., Shroyer, E., and Sutherland, D.: Distributed subglacial discharge drives significant submarine melt at a Greenland tidewater glacier, Geophysical Research Letters, pp. 9328–9336, 2015.

Holland, D. M. and Jenkins, A.: Modeling thermodynamic ice-ocean interactions at the base of an ice shelf, Journal of Physical Oceanography, 29, 1787–1800, 1999.

Holland, D. M., Thomas, R. H., De Young, B., Ribergaard, M. H., and Lyberth, B.: Acceleration of Jakobshavn Isbrae triggered by warm subsurface ocean waters, Nature Geoscience, 1, 659–664, 2008.

Howat, I. M., Joughin, I., and Scambos, T. A.: Rapid changes in ice discharge from Greenland outlet glaciers, Science, 315, 1559–1561, 2007.

Howat, I. M., Joughin, I., Fahnestock, M., Smith, B. E., and Scambos, T. A.: Synchronous retreat and acceleration of southeast Greenland outlet glaciers 2000-06: ice dynamics and coupling to climate, Journal of Glaciology, 54, 646–660, 2008.

Jackson, R. H. and Straneo, F.: Heat, salt, and freshwater budgets for a glacial fjord in Greenland, Journal of Physical Oceanography, 46, 2735–2768, 2016.

Jenkins, A. and Physical, K. N.: Observation and parameterization of ablation at the base of Ronne Ice Shelf, Antarctica, Journal of Physical Oceanography, 40, 2298–2313, 2010.

Joughin, I., Howat, I. M., Smith, B., and Scambos, T.: MEaSUREs Greenland Ice Velocity: Selected Glacier Site Velocity Maps from InSAR, Version 1, 2011.

Joughin, I., Alley, R. B., and Holland, D. M.: Ice-Sheet Response to Oceanic Forcing, Science, 338, 1172–1176, 2012.

Kimball, P., Bailey, J., Das, S., Geyer, R., Harrison, T., Kunz, C., Manganini, K., Mankoff, K., Samuelson, K., Sayre-McCord, T., Straneo, F., Traykovski, P., and Singh, H.: The WHOI Jetyak: An autonomous surface vehicle for oceanographic research in shallow or dangerous waters, in: 2014 IEEE/OES Autonomous Underwater Vehicles (AUV), pp. 1–7, IEEE, 2014.

Kjeldsen, K. K., Khan, S. A., Bjørk, A. A., Nielsen, K., and Mouginot, J.: Ice-dammed lake drainage in west Greenland: Drainage pattern and implications on ice flow and bedrock motion, Geophysical Research Letters, 44, 7320–7327, 2017.

Luckman, A., Benn, D. I., Cottier, F., Bevan, S., Nilsen, F., and Inall, M.: Calving rates at tidewater glaciers vary strongly with ocean temperature, Nature Communications, 6, 8566, 2015.

Mankoff, K. D., Straneo, F., Cenedese, C., Das, S. B., Richards, C. G., and Singh, H.: Structure and dynamics of a subglacial discharge plume in a Greenlandic fjord, Journal of Geophysical Research: Oceans, 121, 8670–8688, 2016.

Meier, M. F. and Post, A.: Fast tidewater glaciers, Journal of Geophysical Research: Atmospheres, 92, 9051–9058, 1987.

Minowa, M., Podolskiy, E. A., Sugiyama, S., Sakakibara, D., and Skvarca, P.: Glacier calving observed with time-lapse imagery and tsunami waves at Glaciar Perito Moreno, Patagonia, Journal of Glaciology, 21, 1–15, 2018.

Moon, T., Joughin, I., Smith, B., and Howat, I.: 21st-Century Evolution of Greenland Outlet Glacier Velocities, Science, 336, 576–578, 2012.

Morton, B. R., Sir Geoffrey Taylor, F. R. S., and Turner, J. S.: Turbulent gravitational convection from maintained and instantaneous sources,
5   Proc. R. Soc. Lond. A, 234, 1–23, 1956.

Nick, F. M., Vieli, A., Howat, I. M., and Joughin, I.: Large-scale changes in Greenland outlet glacier dynamics triggered at the terminus, Nature Geoscience, 2, 110–114, 2009.

Nick, F. M., Vieli, A., Andersen, M. L., Joughin, I., Payne, A., Edwards, T. L., Pattyn, F., and van de Wal, R. S. W.: Future sea-level rise from Greenland's main outlet glaciers in a warming climate, Nature, 497, 235–238, 2013.

10   Rignot, E. and Thomas, R. H.: Mass balance of polar ice sheets, Science, 297, 1502–1506, 2002.

Rignot, E., Xu, Y., Menemenlis, D., Mouginot, J., Scheuchl, B., Li, X., Morlighem, M., Seroussi, H., van den Broeke, M., Fenty, I., Cai, C., An, L., and de Fleurian, B.: Modeling of ocean-induced ice melt rates of five west Greenland glaciers over the past two decades, Geophysical Research Letters, 43, 6374–6382, 2016.

Scambos, T., Sergienko, O., Sargent, A., MacAyeal, D., and Fastook, J.: ICESat profiles of tabular iceberg margins and iceberg breakup at
15   low latitudes, Geophysical Research Letters, 32, 2005.

Silva, T. A. M., Bigg, G. R., and Nicholls, K. W.: Contribution of giant icebergs to the Southern Ocean freshwater flux, Journal of Geophysical Research: Atmospheres, 111, 2006.

Slater, D., Straneo, F., Das, S. B., Richards, C. G., Wagner, T. J. W., and Nienow, P. W.: Three-dimensional fjord circulation doubles ocean melting of a Greenland tidewater glacier, submitted.

20   Slater, D. A., Nienow, P. W., Goldberg, D. N., Cowton, T. R., and Sole, A. J.: A model for tidewater glacier undercutting by submarine melting, Geophysical Research Letters, 44, 2360–2368, 2017.

Stevens, L. A., Straneo, F., Das, S. B., Plueddemann, A. J., Kukulya, A. L., and Morlighem, M.: Linking glacially modified waters to catchment-scale subglacial discharge using autonomous underwater vehicle observations, TC, 10, 417–432, 2016.

Straneo, F. and Cenedese, C.: The Dynamics of Greenland's Glacial Fjords and Their Role in Climate, Annual Review of Marine Science, 7,
25   89–112, 2015.

Veitch, S. A. and Nettles, M.: Spatial and temporal variations in Greenland glacial-earthquake activity, 1993-2010, J. Geophys. Res., 117, F04 007, 2012.

Vieli, A. and Nick, F. M.: Understanding and Modelling Rapid Dynamic Changes of Tidewater Outlet Glaciers: Issues and Implications, Surveys in Geophysics, 32, 437–458, 2011.

30   Wagner, T. J. W., Wadhams, P., Bates, R., Elosegui, P., Stern, A., Vella, D., Abrahamsen, P., Crawford, A., and Nicholls, K. W.: The "foot-loose" mechanism: Iceberg decay from hydrostatic stresses, Geophysical Research Letters, 41, 5522–5529, 2014.

Wagner, T. J. W., James, T. D., Murray, T., and Vella, D.: On the role of buoyant flexure in glacier calving, Geophysical Research Letters, 43, 232–240A, 2016.

Wilson, N., Straneo, F., and Heimbach, P.: Satellite-derived submarine melt rates and mass balance (2011–2015) for Greenland's largest
35   remaining ice tongues, The Cryosphere, 11, 2773–2782, 2017.